Surface & Coatings Technology 516 (2025) 132701

Contents lists available at ScienceDirect

Surface & Coatings Technology

journal homepage: www.elsevier.com/locate/surfcoat

Mechanistic insights into additive-driven dark current and responsivity in organic photodetector with varied film thickness☆

Zhi-Hao Huang [a,b], You-Ren Chen [b], Hou-Chin Cha [c,d], Sheng-Long Jeng [e], Kun-Mu Lee [a,f,g,*], Yu-Ching Huang [a,b,c,f,**]

[a] Department of Chemical and Materials Engineering, Chang Gung University, Taoyuan, 33302, Taiwan
[b] Department of Materials Engineering, Ming Chi University of Technology, New Taipei City, 24301, Taiwan
[c] Organic Electronics Research Center, Ming Chi University of Technology, New Taipei City, 24301, Taiwan
[d] College of Engineering, Ming Chi University of Technology, New Taipei City, 24301, Taiwan
[e] Department of Material Research, National Atomic Research Institute, Taoyuan City 325207, Taiwan
[f] Center for Sustainability and Energy Technologies, Chang Gung University, Taoyuan 33302, Taiwan
[g] College of Environment and Resources, Ming Chi University of Technology, New Taipei City 24301, Taiwan

ARTICLE INFO

Keywords:
Organic photodetectors
Additive
Responsivity
Detectivity
Film thickness
Dark current

ABSTRACT

Organic photodetectors (OPDs) have garnered significant attention due to their advantages of low manufacture cost, high absorption coefficient, tunable energy level, and mechanic flexibility. We selected the low-energy-gap donor material PTB7-Th and the fullerene acceptor $PC_{71}BM$ to form the active layer in a bulk-heterojunction (BHJ) structure, and the aggregation of $PC_{71}BM$ was modulated by adjusting the ratio of the additive 1,8-diiodooctane (DIO). Our investigation focused on both thin and thick film OPDs performance. The addition of DIO enhanced dark current suppression and significantly improved the responsivity, particularly in thin film-based OPDs. Thick film OPDs also exhibited better dark current suppression and responsivity. The best OPD performance was achieved at a reverse bias of −3 V, yielding a noise current of 6.7×10^{-14} A, a responsivity of 0.37 A/W, and a specific detectivity (D_n^*) of 2.94×10^{12} Jones. Notably, the effect of DIO on dark current differs between thick and thin films. The results of this study indicate that noise performance in thick film-based devices is primarily dominated by thermal noise, while changes in surface morphology and structural optimization mainly affect responsivity. Our findings clarify the mechanisms affecting OPD performance and pave the way for the development of high-performance OPDs.

1. Introduction

Organic photodetectors (OPDs) have garnered significant attention due to their low manufacturing cost, ability for solution processing, high absorption coefficients, tunable energy levels, and mechanical flexibility [1–4]. Previous research has shown that the desired performance of broadband OPDs can be achieved by adjusting the surface morphology and thickness of the OPD [5–7]. The selection of the appropriate solvent and the use of additives are key factors in improving bulk heterojunction (BHJ) morphology as well as layer topography [8–10]. The design of narrowband photomultiplication (PM) OPDs relies on precise control of the optical field distribution and active layer thickness to achieve complete absorption of specific wavelengths of light [11,12]. When the active layer thickness increases to about 2.5 μm, incident light with wavelengths shorter than 630 nm can be completely absorbed, enabling the OPD to efficiently detect light signals within this wavelength range [13,14]. Recently, many research groups have developed PM-OPDs exhibiting high charge current density and low dark current [15,16]. This improvement arises from the distinct donor-to-acceptor (D/A) material ratio within the active layer, where the donor material predominantly dictates the behavior. Under dark condition, electron injection from the indium tin oxide (ITO) transparent electrode into the lowest unoccupied molecular orbital (LUMO) of the acceptor material is hindered due to the limited contact interface between the ITO and the

☆ This article is part of a Special issue entitled: 'SDSE 2024' published in Surface & Coatings Technology.

* Corresponding author
** Correspondence to: Y-C. Huang, Department of Materials Engineering, Ming Chi University of Technology, New Taipei City, 24301, Taiwan
E-mail addresses: KMLee@mail.cgu.edu.tw (K.-M. Lee), huangyc@mail.mcut.edu.tw (Y.-C. Huang).

https://doi.org/10.1016/j.surfcoat.2025.132701
Received 31 January 2025; Received in revised form 24 August 2025; Accepted 17 September 2025
Available online 19 September 2025

acceptor material. This reduces the dark current and enhances the signal-to-noise ratio of the devices. Under illumination, energy band bending at the interface, caused by electron trapping in the acceptor material near the electrode, facilitates hole injection from the electrode. Consequently, broadband PM-OPDs can be applied across various wavebands and feature a simple fabrication process, making them a subject of extensive research. However, balancing responsivity, dark current, and film thickness in broadband OPDs is challenging; devices with active layer thicker than 1 μm typically experience difficulties in achieving high responsitivity [17]. Numerous studies have demonstrated that optimizing the morphology of thin active layers can significantly enhance the performance of OPDs, with nanostructures arrangement improving carrier mobility and light absorption efficiency [18,19]. Additionally, morphology control can also reduce trap states and surface recombination, thereby lowering dark current and increasing responsivity [20,21]. OPDs based on thick active layer, however, exhibit various limited factors for performance, such as extended carrier transport paths and increasing recombination losses. Additionally, phase separation within thick films may also cause uneven charge generation and transport, further affecting responsivity and dark current [6,22]. Thus, achieving the high performance of thin films within thick films devices remains a key research focus. Recently, Park et al. developed a broadband OPD with a 1-μm-thick active layer exhibiting high responsivity and low dark current [23]. OPDs consisting of PBDTT-8ttTPD and $PC_{71}BM$ achieved a low dark current of 3.72×10^{-9} A/cm^2 and high responsivity of 0.39 A/W, attributed to the well-controlled morphology, high molar absorption coefficient, and excellent carrier mobility of the PBDTT-8ttTPD:$PC_{71}BM$ layer. Consequently, the specific detectivity (D_n*) of the PBDTT-8ttTPD-based OPD devices reached 1.13×10^{13} Jones at −2 V. Despite the progress, studies comparing the impacts of thin and thick films on OPD performance are limited, particularly regarding the effects of additives in thick films.

To investigate the effects of thin and thick films on the performance of OPDs, we selected a widely-used system and employed additives to modify its morphology and structure. Among low bandgap polymer-based BHJ OPDs, the polymer poly[4,8-bis(5-(2-ethylhexyl)thiophen-2-yl)benzo[1,2-b;4,5-b']-dithiophene-2,6-diyl-alt-(4-(2-ethylhexyl)-3-fluorothieno[3,4-*b*]thiophene-)-2-carboxylate-2-6-diyl] (PTB7-Th), used as the donor material, exhibits many excellent device performance characteristics [24–27]. Its morphology notably influences carrier lifetime performance [28,29], and its good mobility and energy level matching make it one of the most outstanding systems for visible-near infrared applications. We used the blend of PTB7-Th and the fullerene derivatives, [6,6]-phenyl-C71-butyric acid methyl ester ($PC_{71}BM$), as the active layer in a BHJ structure. The acceptor material, $PC_{71}BM$, improved device performance by reducing bimolecular recombination, an effect attributed to significant changes in the active layer morphology [30]. Recent studies have shown similar results, demonstrating that enhancing the crystallinity and morphological orientation of PTB7-Th through a binary additive can suppress charge carrier recombination [27], emphasizing the role of PCBM influencing both performance and morphology of solar cells. The aggregation of $PC_{71}BM$ was modulated by adjusting the concentration of the additive 1,8-diiodooctane (DIO). However, most studies have focused on optimizing the DIO ratio for thin active layers. In thick active layers, the high boiling point of the DIO can lead to residual additive embedded within the active layer, potentially exerting a greater impact on the nanostructure within. This work explores these phenomena and their underlying mechanisms in detail. In this study, we examine how variations in active layer thickness influence dark current density (J_d) and responsivity under a bias of −3 V, implementing BHJ thin-film and thick-film structures accordingly. We revisited the straightforward adding additives approach to provide insight into the favorable structure and morphology in both thin and thick films. Enhanced interfacial interactions were analyzed by impedance measurement, while the BHJ structure improvements were characterized using grazing-incidence wide-angle X-ray scattering (GIWAXS). These results provide a more comprehensive understanding of the influencing factors of the performance of OPDs.

2. Materials and methods

2.1. Materials

PTB7-Th and $PC_{71}BM$ were purchased from 1-Material Inc. and Lumtec, respectively. Zinc acetate was obtained from Alfa Aesar. 2-Methoxylethanol, ethanolamine, chlorobenzene (CB), 1,8-diiodooctane (DIO) and MoO_3 were acquired from Sigma–Aldrich. All reagents and solvents were used without further purification. The chemical structures of PTB7-Th, and $PC_{71}BM$ are presented in Fig. 1(a). ZnO was synthesized through the sol-gel method, according to a previous report [31]. The PTB7-Th:$PC_{71}BM$ active layer solution (1:1.5, 20/25/35/45 mg/ml in chlorobenzene with 0–10 vol% DIO) was stirred at 65 °C for 12 h in a glove box.

2.2. Device fabrication

The OPD was fabricated on a commercially available indium tin oxide (ITO)/glass substrate that was pre-cleaned by ultrasonication in deionized water, acetone, and isopropanol, each for 30 min consecutively. The as-prepared ZnO, electron transport layer (ETL), was then deposited onto the ITO/glass substrate by spin coating at 3000 rpm for 30 s, followed by annealing treatment at 170 °C for 20 min. Subsequently, the substrates were transferred to an N_2-filled glovebox. Active layers with various thicknesses were deposited onto the ZnO layers by spin-coating at rotation speeds of 100, 250, 500, 1000, 2000, and 5000 rpm for 40 s in a nitrogen-filled glove box, with ~45 μL of active layer solution dispensed per cycle. Thick films (>1 μm) were prepared by spin-coating at 100 and 250 rpm, followed either by vacuum treatment for 4 h or by extended spin-coating for 10 min until complete solvent evaporation was achieved. Subsequently, MoO_3 as hole transport layer (HTL, 7 nm) and Ag (100 nm) were successively deposited onto the active layer through thermal evaporation. The OPDs device area was 0.04 cm^2, and the corresponding energy band diagram of the OPD structure is shown in Fig. 1(b).

2.3. Device characterization

The dark current density (J_d) of the device was recorded using a Keithley 2400 source meter. The current density–voltage (J–V) characteristics and noise current measurements were conducted using a programmable source meter, the Keithley 2636A model. To study the response of the photocurrent to light intensity, a light-emitting diode (LED; Thorlabs, M530L2) with a wavelength of 530 nm was directed through a motorized filter wheel (Thorlabs, FW102CNEB), and the light intensity was controlled by evaluating the linear dynamic range (LDR). For frequency response measurements, a commercial LED (Thorlabs) with a wavelength of 530 nm and a luminous flux density of 1 mW/cm^2 was employed. The LED was connected to a Tektronix AFG3102C function generator to produce pulses that triggered the OPD. The output pulses from the OPD were amplified using a preamplifier with a voltage gain factor of 10^6, and the amplified signals were captured and analyzed by a 2.5 GHz oscilloscope (Teledyne LeCroy, WaveRunner 625Zi). The thickness of the film was measured using an Alpha-stepper (Bruker), while the surface morphology and roughness of the film were analyzed by atomic force microscopy (AFM; Bruker). A UV–Vis spectrophotometer (Jasco V-750) was used to study the absorption behavior of the active layer and to calculate its bandgap energy. Additionally, electrochemical impedance spectroscopy (EIS; Solartron, Materials Lab XM) was employed to examine the impedance in the frequency range of 10^{-1} MHz to 1 MHz, applying a sinusoidal AC signal with an amplitude of 1 V. Transient photovoltage (TPV) and transient photocurrent (TPC) measurements were performed using the Paios 4.0 system from FLUXiM AG

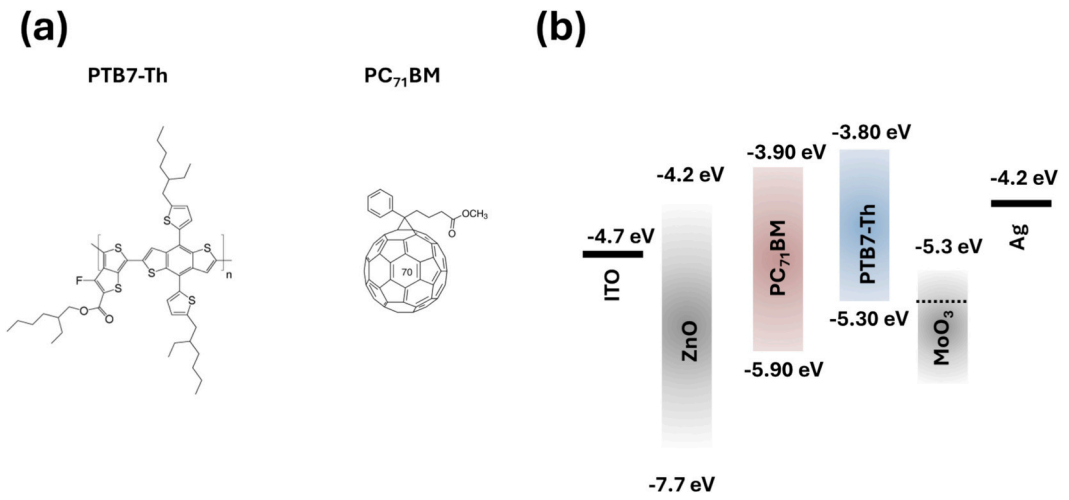

Fig. 1. (a) Chemical structures of PTB7-Th and $PC_{71}BM$. (b) Schematic energy band diagram of the OPD device.

to determine the charge carrier extraction time and recombination rates.

For the GIWAXS measurements, samples were prepared on silicon wafer substrates and analyzed at the 23A beamline station of the National Synchrotron Radiation Research Center (NSRRC) in Taiwan. A monochromatic X-ray beam with an energy of 10 keV (wavelength 1.2398 Å) was used, with the incident angle precisely aligned to 0.2° for each sample. The wide-angle scattering signals were collected by a C10158DK flat-panel detector with 2352 pixels, placed 19.5 cm from the sample, and the data collection time for each measurement was 50 s. Radial slices were taken from the 2D GIWAXS patterns to extract simplified 1D curves in both the out-of-plane (Qz, perpendicular to the film surface) and in-plane (Qx, parallel to the film surface) directions. These 1D curves were obtained by performing radial integrations of the azimuthal angles from 90° to 110° and polar angles from 160° to 180°, highlighting the diffraction features of polymer/BHJ crystallites with different orientations.

3. Results

3.1. Effect of active layer thickness on OPD performance

The dark current (J_d) of the devices is significantly affected by the thickness of the active layer (AL). We first controlled the AL thickness (200–1500 nm) to find the optimum On/Off ratio. The J_d of PTB7-Th:$PC_{71}BM$ devices were evaluated at −3 V to 1.5 V, as shown in Fig. 2 (a). As the thickness of the PTB7-Th:$PC_{71}BM$ film increased from 70 nm to 1500 nm, J_d decreased gradually from 4.9×10^{-4} A/cm^2 to 4.1×10^{-7} A/cm^2 at −3 V, respectively. When the AL thickness exceeds 1 μm, the

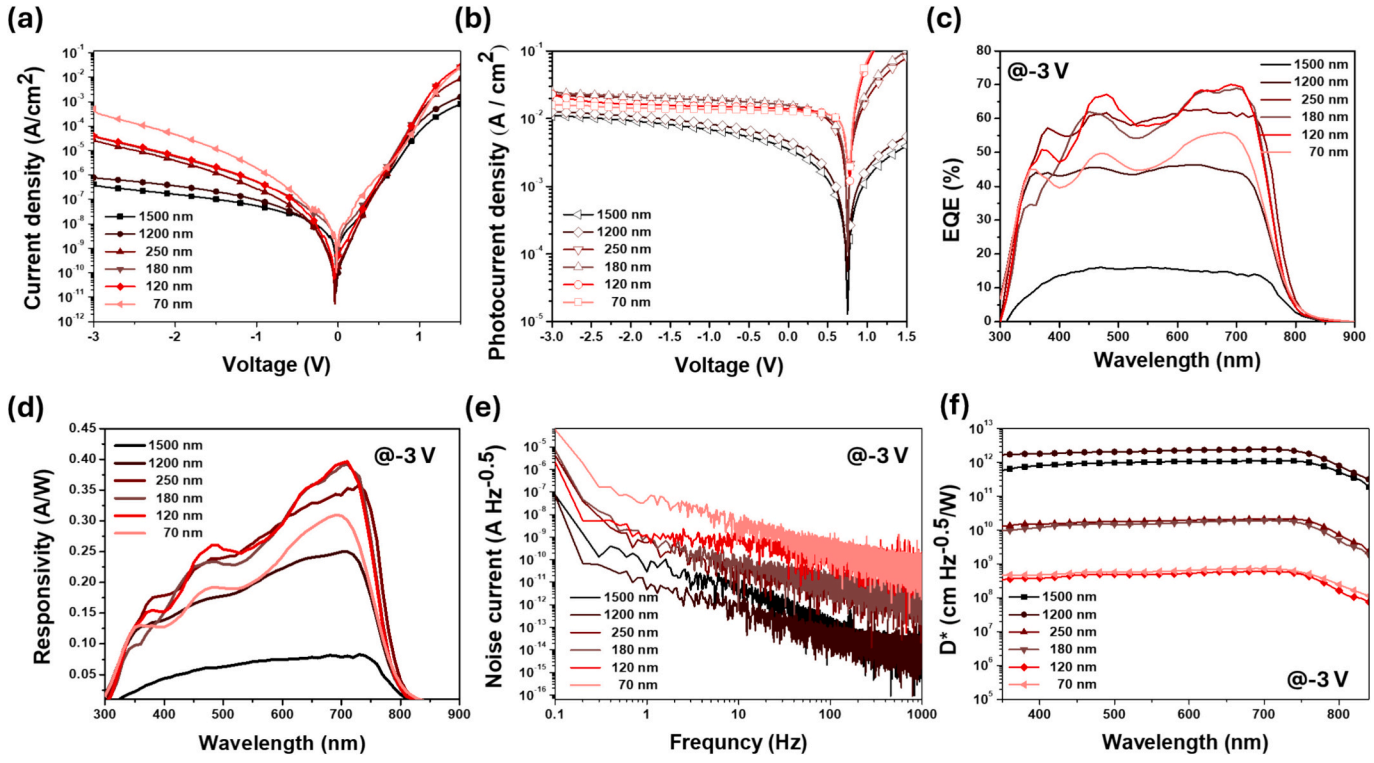

Fig. 2. (a) J_d-V curves, (b) photocurrent density, (c) EQE spectrum, (d) responsivity spectrum, (e) noise current and (f) specific detectivity spectrum of OPDs with different thicknesses of 1500 nm, 1200 nm, 250 nm, 180 nm, 120 nm and 70 nm.

dark current significantly decreases by 2 to 3 orders of magnitude. Fig. 2 (b) presents a plot of the simulated short-circuit photocurrent density (J_{sc}) under −3 V bias, allowing us to evaluate the degree of charge extraction. The J_{sc} reached a maximum of 2.49×10^{-2} A/cm^2 at an AL thickness of 180 nm and then slightly decreased to 1.26×10^{-3} A/cm^2 at an AL thickness of 1200 nm. The current reaches saturation at a bias of −3 V, indicating that when the AL thickness exceeds 1 μm, a bias voltage of −3 V is required for effective carrier extraction. Therefore, we evaluated the EQE and responsivity at a bias of −3 V in Fig. 2(c-d). The EQE and responsivity spectra exhibit broadband coverage over visible wavelengths (300–780 nm), with primary peaks at 500 and 700 nm. As the AL thickness increases, the characteristic peaks transition into a flat spectrum. For devices with a 120 nm AL thickness, the EQE and responsivity at 700 nm were 69 % and 0.393 A/W, respectively. With an increase in AL thickness to 1500 nm, the EQE and responsivity decreased to 13.8 % and 0.078 A/W, respectively. A crucial performance metric for OPDs is specific detectivity (D_n*), which quanifies the OPDs' sensitivity to detect the minimal signal levels [32]. The decrease in D_n* with increasing AL thickness results from reduced responsivity and higher dark current, both of which lower the overall signal-to-noise ratio. [24,33]. To avoid this, all current noise components must be carefully calculated, including shot noise, thermal noise, and flicker noise (1/f). The flicker noise, or 1/f noise, significantly impacts low frequency operation [34] but becomes negligible at frequencies beyond 100 Hz [35]. Conversely, shot noise and thermal noise (Johnson noise) are considered as white noise sources [36]. The root-mean-square (RMS) white noise (In, $_{RMS}$) was calculated using Eq. (1) [37,38]:

$$I_{n,RMS} = \sqrt{\int_{f1}^{f2} i_n^2 df} \quad (1)$$

where the lower (f1) and upper (f2) frequencies were set to 100 Hz and 1 kHz, respectively. This interval corresponds to the flat white noise region between the 1/f corner and the high-frequency roll-off [39], ensuring that the integrated value accurately reflects the intrinsic white noise contribution. In this study, we did not examine the effect of flicker noise on the OPDs. The measured white noise currents at −3 V bias for devices with varying AL thickness ranged between 1.5×10^{-10} to 4.1×10^{-14} A (Fig. 2(e)). When the AL thickness increased to 1200 nm and 1500 nm, the change in noise current remained minimal. Fig. 2(f) presents the D_n*, which is the signal-to-noise ratio derived from the responsivity and dark current noise. D_n* can be evaluated using the following equation, Eq. (2) [33]:

$$D_n^* = \frac{R\sqrt{A\Delta f}}{i_n} \quad (2)$$

where R is the responsivity (A/W), A (cm^2) is the device area, Δf (Hz) is the detection bandwidth, and i_n (A) is the white noise current in dark conditions. Fig. S1 illustrates the linear dynamic range (LDR) of the device measured at 0 V under a 530 nm LED light source. For the AL thicknesses of 70, 120, 180, 250, 1200, and 1500 nm, the respective LDRs were measured as 99, 105, 105, 98, 97, and 96 dB. The decreasing slope of the LDR as the AL thickness increases represents the loss of charge. Table 1 lists the data for OPDs with different AL thicknesses, including dark current, EQE, responsivity, RMS white noise, D_n*, and LDR. These results show the influence of AL thickness on device characteristics, particularly the notable divergence between photocurrent and dark current when the AL thickness surpasses 1 μm. Consequently, we selected a thin film with an AL thickness of 70 nm and a thick film of 1200 nm for the further comparative studies on additive optimization.

3.2. Characterization of thick film and thin film OPD with different proportions of additives

To obtain OPDs with different additive ratios in both thick (1200 nm) and thin (70 nm) ALs, we first evaluated the relationship among spin coating rate, additive concentrations and film thickness (Fig. S2). When the spin speed is kept below 250 rpm, a substantial amount of solution remains on the ZnO substrate, yielding a film thickness exceeding 1 μm after vacuum drying. The film thickness slightly increases with the increasing the DIO additive, largely because the high boiling point of DIO slows the solvent drying rate, allowing more material to settle and impacting the overall thickness of the film. To investigate the influence of additives on OPD performance in both thin and thick AL films, we fabricated OPDs with varying DIO concentrations and compared their performances. In Fig. 3(a), the effect of different additive concentrations on the J_d of OPDs with thin AL (thin-AL-based OPDs) is shown. In comparison to OPDs without DIO, OPDs with 3 vol% DIO showed a reduced J_d from 4.9×10^{-4} A/cm^2 to 3.5×10^{-7} A/cm^2 at −3 V. However, DIO concentrations over 5 vol% caused an increase in J_d, possibly due to excessive phase separation of AL. Therefore, only OPDs with 0, 3 and 10 vol% DIO concentrations were evaluated further. Fig. 3 (b) and (c) show the EQE and responsivity spectrum of the thin AL-based OPDs with 0, 3, and 10 vol% DIO. OPDs without DIO demonstrated an EQE of 54.6 % and a responsivity of 0.308 A/W, whereas those with 3 vol% DIO exhibited an increased EQE of 62.7 % and a responsivity of 0.353 A/W at 700 nm. Due to the thin AL, external electric field influence remains dominant, minimizing the effect of additives on charge extraction under bias. Fig. 3(d) highlights the noise current reductions achieved with DIO, where 3 vol% DIO resulted in a decrease to 1.4×10^{-12} A, while higher DIO concentration (10 vol%) increased the noise current to 5.4×10^{-12} A. The D_n* for thin-AL-based OPDs, shown in Fig. 3(e), peaked at 7.98×10^{10} Jones for 3 vol% DIO under −3 V at 700 nm. These results, summarized in Table 2, indicates that the DIO effectively reduces J_d and enhances the responsivity and D_n*of the thin-AL-based OPDs. For thick-AL-based OPDs, Fig. 4(a) shows a minimal effect of DIO on J_d, an obvious contrast to the behavior of the thin-AL-based OPDs. Fig. 4(b) and (c) demonstrate improvements in EQE and responsivity of thick-AL-based OPDs with increasing DIO, achieving a highest EQE of 65.6 % and responsivity of 0.370 A/W. In Fig. 4(d), the noise currents of thick-AL-based OPDs with various DIO concentrations are stable, approximately 4×10^{-14} A at −3 V, aligning with the consistent J_d. The highest D_n* of thick-AL-based AL with 3 vol% DIO shown in Fig. 4(e) was 2.94×10^{12} Jones at −3 V and 700 nm. All results are listed in Table 3, and these results demonstrate that DIO improves EQE and responsivity in thick films without significantly affecting dark current or noise current, underscoring the distinct influence of additive

Table 1
Performance characteristics of OPDs with different thicknesses.

Thickness (nm)	J_d [a] (A/cm^2) @-3 V	EQE (%)	Responsivity (A/W)	Noise_rms[a] (A) @-3 V	D_n* (Jones)	LDR[b] (dB)
1500	4.1×10^{-7} ($5.1 \pm 1.0 \times 10^{-7}$)	13.8	0.078	5.1×10^{-14} ($5.6 \pm 0.5 \times 10^{-14}$)	1.08×10^{12}	96
1200	7.8×10^{-7} ($8.5 \pm 0.7 \times 10^{-7}$)	44.2	0.249	4.1×10^{-14} ($4.4 \pm 0.3 \times 10^{-14}$)	2.41×10^{12}	97
250	2.6×10^{-5} ($3.0 \pm 0.4 \times 10^{-5}$)	60.5	0.341	5.5×10^{-12} ($5.8 \pm 0.3 \times 10^{-12}$)	2.10×10^{10}	98
180	3.8×10^{-5} ($4.2 \pm 0.5 \times 10^{-5}$)	68.9	0.389	6.5×10^{-12} ($6.9 \pm 0.4 \times 10^{-12}$)	1.91×10^{10}	104
120	3.8×10^{-5} ($4.3 \pm 0.5 \times 10^{-5}$)	69.8	0.393	2.0×10^{-10} ($2.5 \pm 0.5 \times 10^{-10}$)	6.06×10^{8}	105
70	4.9×10^{-4} ($5.4 \pm 0.5 \times 10^{-4}$)	54.6	0.308	1.5×10^{-10} ($1.9 \pm 0.4 \times 10^{-10}$)	7.30×10^{8}	99

[a] The average data are obtained from 10 devices for OPD.
[b] The values correspond to the LDR of the device with bias 0 V.

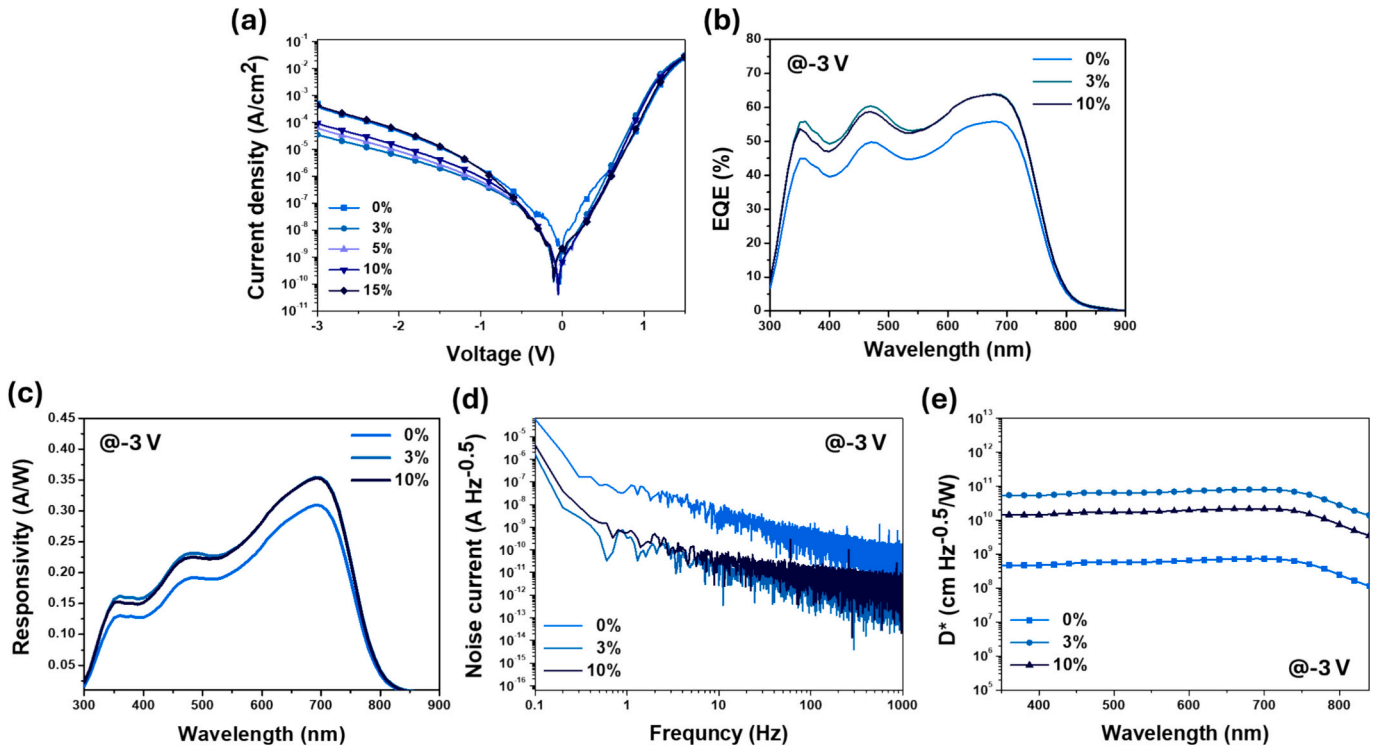

Fig. 3. (a) J_d -V curves, (b) EQE spectrum, (c) responsivity spectrum, (d) noise current, and (e) detectivity spectrum of thin-AL-based OPDs with different DIO concentrations (0 %, 3 %, 10 %).

Table 2
Performance characteristics of thin-AL-based OPDs fabricated with different DIO concentrations.

DIO (%)	J_d [a] (A/cm^2) @-3 V	EQE (%)	Responsivity (A/W)	Noise_rms[a] (A) @-3 V	D_n* (Jones)	LDR[b] (dB)
0	4.9×10^{-4} ($5.4 \pm 0.5 \times 10^{-4}$)	54.6	0.308	1.5×10^{-10} ($1.9 \pm 0.4 \times 10^{-10}$)	7.30×10^{8}	/
3	3.5×10^{-5} ($3.8 \pm 0.3 \times 10^{-5}$)	62.7	0.353	1.4×10^{-12} ($1.8 \pm 0.4 \times 10^{-12}$)	7.98×10^{10}	17.4
10	9.2×10^{-5} ($9.5 \pm 0.3 \times 10^{-5}$)	62.4	0.352	5.4×10^{-12} ($5.9 \pm 0.5 \times 10^{-12}$)	2.17×10^{10}	8.2

[a] The average data were obtained from 10 OPD devices.
[b] The values correspond to the LDR of the device at a bias of -3 V.

across film thicknesses. Fig. S3 illustrates the LDR for both thin-AL and thick-AL based OPDs at −3 V, where the thick-AL-based OPDs with 3 vol % DIO achieved an LDR of 62.0 dB. The high LDR in the thick AL confirms that the dark current injection can be effective suppressed at −3 V, maintaining performance. To clarify the origin of dark current in thin and thick ALs, we estimated the shunt resistance (R_{sh}) by linearly fitting the dark current-voltage curve, focusing on the region between 0 and 0.2 V (Fig. S4). Previous studies have shown that trap states and energetic disorder near the band edges can enhance thermally generated dark current by facilitating sub-bandgap absorption and thermal carrier generation within the active layer [3,40]. Such tail-state disorder increases the density of thermally activated carriers, which, together with variations in carrier transport pathways, may lead to a stronger dependence of dark current on the active layer thickness. In addition, the thermal noise current was estimated using Eq. (3) [41], providing further insight into the contribution of thermal fluctuations to the overall noise characteristics.

$$i_{thermal} = \sqrt{\frac{4kTB}{R_{sh}}} \tag{3}$$

where B (1 Hz) is the normalized bandwidth, k is the Boltzmann constant (1.38×10^{-23} J/K), T (K) is the temperature, and R_{sh} (Ω) is the shunt resistance of the OPDs. The R_{sh} value is estimated from the linear fit of the dark current-voltage curve [42,43], as shown in Fig. S4. We represented the calculated thermal noise and the measured noise current using a statistical chart (Fig. S5) and summarized the data in Table S1. For the thin-AL-based OPDs, the R_{sh} was measured to be around 10^{10} Ω, with thermal noise current around 10^{-16} A, which is much lower than the measured noise current, suggesting that the shot noise dominates in thin films. In contrast, the shunt resistance of the thick-AL-based OPDs was approximately 10^{8} Ω, with thermal noise around 10^{-15} A, comparable to the measured noise current at -3 V, indicating that the thermal noise likely dominates in thick films. Additionally, we assessed the effective energy gap of the material by examining the optical absorption of both thin and thick films, as it affects the dark current in the thick film system. These observations underscore the role of thermal noise in influencing dark current in thick films, while shot noise is predominant in thin-AL-based OPDs. To further investigate the effect across a wide thickness range (300–1900 nm), we provide additional results in Fig. S6 (a–c). By increasing the solution concentration from 25 mg/ml to 45 mg/ml, intermediate-thickness films (300–800 nm) were obtained, enabling a systematic study in the technologically relevant regime. In this regime, the dark current decreased by approximately two orders of magnitude, with the optimal EQE observed at a thickness of ~550 nm. In addition, films were also prepared by spin-coating at a low speed of 250 rpm for 10 min until completely dried. This approach avoids the use of vacuum drying and eliminates potential differences in crystallization kinetics. For thick films (1100–1900 nm), the results are consistent with those obtained using vacuum drying, with the device having an active

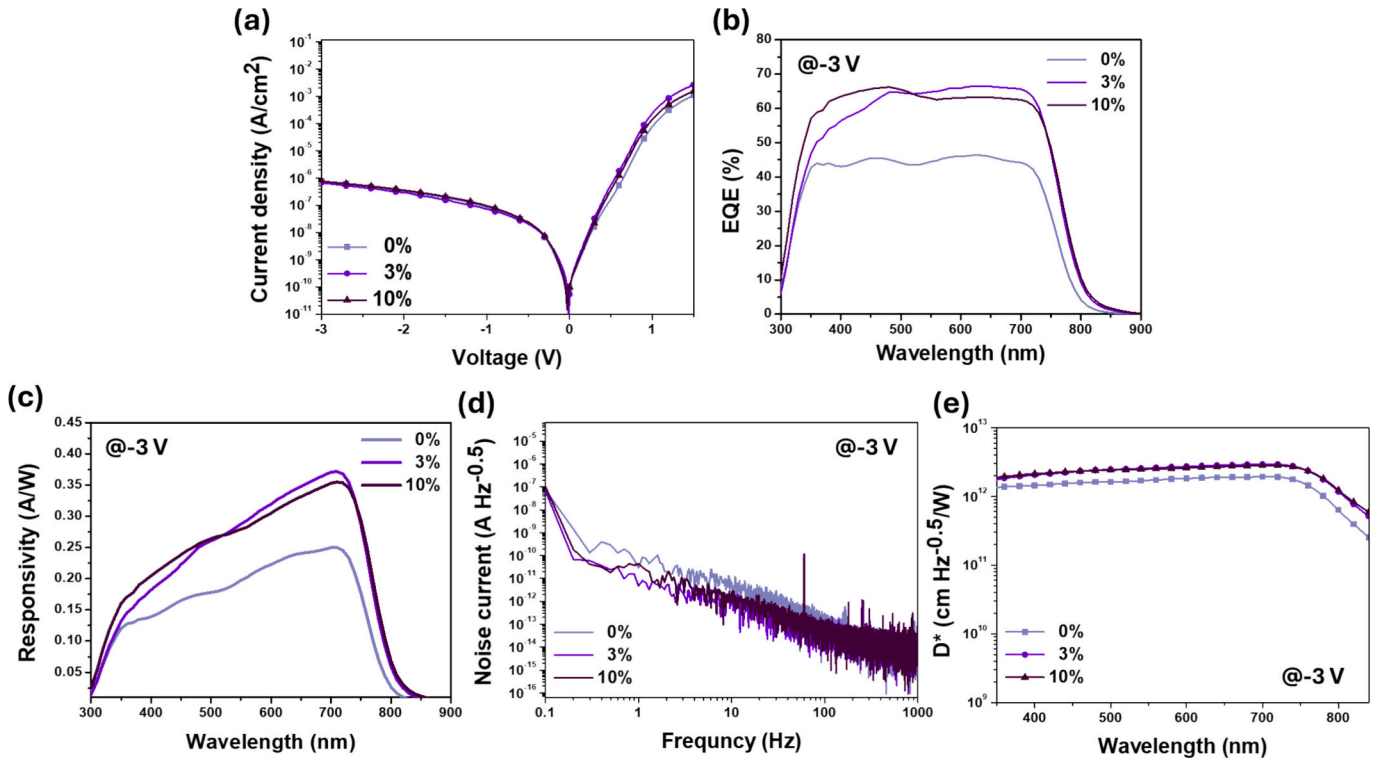

Fig. 4. (a) J_d -V curves, (b) EQE spectrum, (c) responsivity spectrum, (d) noise current, and (e) detectivity spectrum of thick-AL-based OPDs with different DIO concentrations (0 %, 3 %, 10 %).

Table 3
Performance characteristics of thick-AL-based OPDs fabricated with different DIO concentrations.

DIO (%)	J_d [a] (A/cm^2) @-3 V	EQE (%)	Responsivity (A/W)	Noise_rms[a] (A) @-3 V	D_n* (Jones)	LDR[b] (dB)
0	7.6×10^{-7} ($8.0 \pm 0.4 \times 10^{-7}$)	44.2	0.249	5.1×10^{-14} ($5.6 \pm 0.5 \times 10^{-14}$)	1.93×10^{12}	37.6
3	6.7×10^{-7} ($7.0 \pm 0.3 \times 10^{-7}$)	65.6	0.370	4.1×10^{-14} ($4.6 \pm 0.5 \times 10^{-14}$)	2.94×10^{12}	62.0
10	7.8×10^{-7} ($8.1 \pm 0.3 \times 10^{-7}$)	62.5	0.352	4.2×10^{-14} ($4.8 \pm 0.6 \times 10^{-14}$)	2.73×10^{12}	49.7

[a] The average data were obtained from 10 OPD devices.
[b] The values correspond to the LDR of the device at a bias of -3 V.

layer thickness of 1100 nm exhibiting the most favorable trade-off between responsivity and dark current suppression. As shown in Fig. S6 (d–f), we conducted a more precise verification of the additive ratio in the 1100 nm films. We further examined DIO contents of 1.5 %, 3 %, and 4.5 %, and confirmed that 3 % DIO provides the optimal performance. Importantly, the influence of DIO additives on thick films remains consistent regardless of whether the films were vacuum-dried or spin-coated until complete solvent evaporation was achieved.

We further investigated the optical, morphological, and structural characteristics of thick and thin ALs to better understand the effects of additive concentration and AL thickness on OPDs' performance. As shown in Fig. S7(a–b), the UV–visible absorption spectra reveal the broad absorption of PTB7-Th:$PC_{71}BM$ across 300–800 nm, with a maximum peak centered at ~705 nm. Compared with thin ALs, thick ALs exhibit stronger absorption, particularly in the 500–800 nm region, where higher DIO concentrations further enhance the absorption intensity. Moreover, a slight red-shift of the absorption peak suggests improved molecular ordering and enhanced crystallinity of the PTB7-Th domains induced by the DIO additive. To further examine the influence of DIO concentration, Fig. S7(c) presents the absorption spectra of ~550 nm-thick ALs at different additive ratios (0 %, 1.5 %, 3 %, 4.5 %) without normalization. The results confirm that increasing DIO content intensifies the overall absorption and slightly shifts the spectra toward longer wavelengths, providing direct evidence that DIO not only improves film morphology but also promotes more efficient light harvesting in OPDs.

Fig. S8 demonstrates the insight into the surface morphology differences between the thin and thick ALs by using atomic force microscopy (AFM). Without DIO, both AL thicknesses displayed uneven morphologies due to PCBM aggregation. However, the addition of 3 % DIO led to relatively smooth morphologies by mitigating the PCBM aggregation. In thick AL, the morphology was more sensitive to DIO concentration changes; at 10 % DIO, excessive phase separation increased surface roughness (Fig. S7(f)). To determine the effect of DIO on the molecular ordering, grazing incidence wide-angle X-ray scattering (GIWAXS) was employed on the thin and thick ALs with various DIO concentrations. The 2D GIWAXS patterns and 1D profiles, presented in Fig. 5, demonstrate a pronounced peak at $q_{xy} = 2.8$ nm^{-1} in the in-plane direction, corresponding to the (100) lamellar stacking of PTB7-Th. A peak around $q \approx 13.1$ nm^{-1} corresponds to the aggregation of PC_{71} BM, which is stronger in thick film without DIO, suggesting that $PC_{71}BM$ aggregation dominates the crystallization. In the out-of-plane direction (Fig. 5(f)), a broad diffraction peak at $q_z = 12 \sim 20$ nm^{-1} is due to the convolution of the (010) stacking peaks of PTB7-Th and $PC_{71}BM$. In pure PTB7-Th and $PC_{71}BM$ films (Fig. S9 and Fig. S10), two peaks located at approximately 13.5 and 16.5 nm^{-1}, corresponding to the PCBM peak and the PTB7-Th peak, respectively. In the BHJ films, the position of the convolution of the (010) stacking peaks is related to the degree of $PC_{71}BM$ aggregation. Without additives, crystallization is primarily dominated by $PC_{71}BM$ [44,45]. The addition of 3 vol% DIO

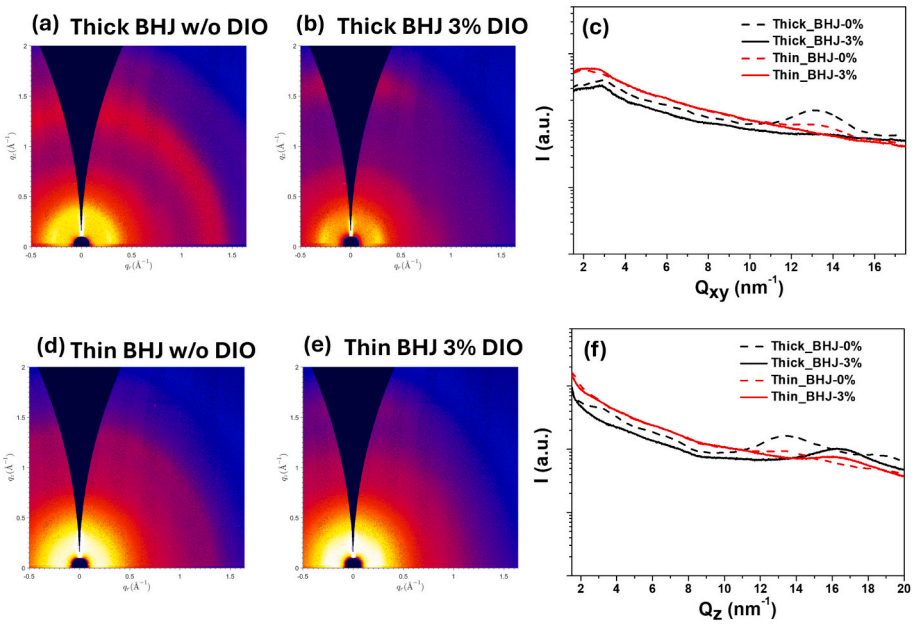

Fig. 5. 2D GIWAXS patterns for (a, b) thin and (d, e) thick film systems in the BHJ with different DIO concentrations (0 %, 3 %). 1D GIWAXs profiles of (c) in-plane Q_{xy} and (f) out-of-plane Q_z for BHJ thin and thick film systems with different DIO concentrations (0 %, 3 %).

reduced $PC_{71}BM$ aggregation and increased the intensity of the (010) stacking peak at $q_z = 16.5\ nm^{-1}$ in thick films compared to thin ones. This effect highlights that, in thick films, DIO promotes PTB7-Th ordering and diminishes PCBM crystallization. These observations illustrate that DIO significantly alters the morphology and crystallinity in thick and thin ALs, enhancing structural order in thick films while controlling phase separation.

Moreover, we conducted electrochemical impedance spectroscopy (EIS) to precisely investigate the interfacial resistance and charge behavior in OPDs with varying AL thickness and DIO concentrations. The Nyquist plots shown in Fig. S11(a-d) display two distinct semi-circular arcs: one at high frequencies (left-hand side), associated with charge transport, and another at low frequencies (right-hand side), related to charge recombination. [46,47]. Also, the diameter of the semicircle extending along the real axis represents the influence of charge transport resistance, where higher charge transport resistance leads to a reduction of J_d. As shown in the inset of Fig. S11 (a), the OPD can be modeled by an equivalent circuit consisting of an internal series resistance (R_S), a charge transport resistance (R_{CT}), and a constant phase element (CPE). In dark condition, the thick-AL-based OPD exhibits higher R_{CT} compared to the thin-AL-based OPDs, indicating that the increased thickness improves interfacial contact and charge transport behavior, reducing leakage current and J_d. Under illumination, however, the R_{CT} values for both thin-AL and thick-AL-based OPDs were comparable, indicating effective interfacial contact and charge transport, thus boosting photo-responsivity in thick ALs with DIO. Fig. S11 (e-f) shows that the thick-AL-based OPDs exhibits a lower capacitance value in the dark, with the best value being approximately 0.4 nF. Under illumination, these films facilitates carrier extraction, consistent with the resistance and capacitance trends observed in Fig. S11 (a-d). However, the EIS results differed from the noise current trend, aligning with our hypothesis that noise current in thick ALs is primarily dominated by thermal noise rather than by capacitance. Fig. 6 illustrates the differences between thin and thick ALs, indicating stronger crystallinity in thicker ALs, which enhances carrier transport under bias and suppresses dark current. The TPC and TPV measurements were used to investigate the intrinsic characteristics of the charge extraction process and charge recombination kinetics [48], as shown in Fig. S12 (a-b).) After DIO incorporation, the TPV results show that the carrier extraction time

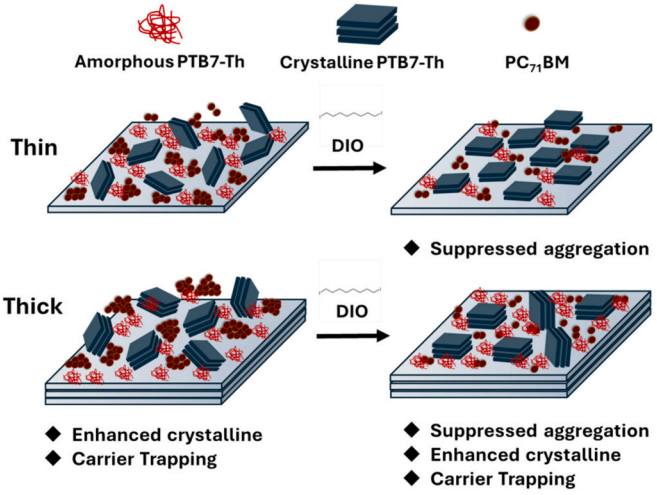

Fig. 6. Schematic representation of the morphology of thin and thick active layer with different DIO concentrations.

decreased from 0.66 μs to 0.61 μs for the thin-AL-based OPDs and from 1.3 μs to 0.71 μs for the thick-AL-based OPDs, respectively. This faster extraction indicates that $PC_{71}BM$ aggregation impedes charge extraction more in thin films. Additionally, TPV measurements reveal that the carrier recombination lifetime increased from 118 μs to 131 μs for the thin-AL-based OPDs, and from 26 μs to 174 μs for the thick-AL-based OPDs, respectively. This prolonged recombination lifetime suggests improved crystallinity and reduced energy loss, particularly in thick films. In summary, the results of charge extraction and recombination behavior confirm that the addition of DIO in thick ALs promote a more crystalline BHJ structure, lowering recombination and enhancing responsivity under bias.

The response speed of the OPDs and its dependence on dark current were further evaluated under a bias of −3 V. As shown in Fig. S13(a–c), the thin-film device exhibited a rise time of 3.5 μs and a fall time of 4.0 μs, while the thick-film device showed faster dynamics with a rise time of 0.4 μs and a fall time of 1.5 μs. The response was stable over 10

consecutives on–off cycles of LED illumination at 530 nm, confirming the good reproducibility of devices. Furthermore, the −3 dB bandwidth measurements in Fig. S13(d) revealed that the cutoff frequency depends on active layer thickness. The f_{-3dB} is closely related to the resistor–capacitor (RC) time constant of the equivalent circuit and the carrier transit time [49]. The series resistance (R) was extracted from the differential of the J–V curve [50], giving R ≈ 120 Ω for the 1100 nm thick-film device, while the capacitance was estimated to be ~0.4 nF. Based on $f_{RC} = 1/(2\pi RC)$, the RC-limited speed was calculated to be 3.31 MHz, corresponding to a τ_{tr} of ~0.4 μs. The carrier-transit-limited frequency (f_{tr}) = $3.5/(2\pi\tau_{tr})$ was further estimated to be ~1.39 MHz. Since $1/f_{-3dB}^2 = 1/f_{tr}^2 + 1/f_{RC}^2$, the calculated cutoff frequency is ~1.28 MHz, which is in close agreement with the measured result (1.04 MHz). Importantly, the device with AL thickness of 1100 nm exhibited the highest cutoff frequency, while further increasing the thickness led to a significant drop in f_{-3dB}, which can be attributed to slow carrier extraction. These results highlight the inherent trade-off between dark current suppression and response speed in OPDs with different AL thicknesses.

4. Conclusions

This study demonstrates that the performance of OPDs can be significantly enhanced by adjusting the additive concentration in the active layer. Using PTB7-Th as the donor material and $PC_{71}BM$ as the acceptor in a BHJ structure, we explored the impact of the additive DIO on both thin and thick active layers. Our findings reveal that DIO not only suppresses dark current but also improves responsivity, particularly in thin film OPDs. For thick film OPDs, while thermal noise primary influences noise performance, improvements in surface morphology and structural are critical for enhancing responsivity. The best performance of OPDs was achieved at a reverse bias of −3 V, with a noise current of 6.7×10^{-14} A, a responsivity of 0.37 A/W, and a specific detectivity (D_n*) of 2.94×10^{12} Jones. These results highlight the different dependencies of thick-AL and thin-AL-based OPDs on DIO concentrations for optimizing dark current and responsivity. By clarifying these influencing mechanisms, our study paves the way for developing high-performance OPDs tailored to specific applications through precise optimization.

CRediT authorship contribution statement

Zhi-Hao Huang: Writing – original draft, Visualization, Validation, Formal analysis, Data curation. **You-Ren Chen:** Validation, Formal analysis, Data curation. **Hou-Chin Cha:** Writing – review & editing, Writing – original draft, Visualization. **Sheng-Long Jene:** Writing – original draft, Visualization. **Kun-Mu Lee:** Writing – review & editing, Supervision, Resources, Project administration, Funding acquisition. **Yu-Ching Huang:** Writing – review & editing, Validation, Supervision, Resources, Project administration, Methodology, Funding acquisition, Conceptualization.

Declaration of competing interest

The authors declare that they have no known competing financial interests or personal relationships that could have appeared to influence the work reported in this paper.

Acknowledgments

The financial supports from the National Science and Technology Council of Taiwan (Grant Nos. NSTC 111-2223-E-182-001- MY4, 112-2628-E-131-001-MY4, 114-2622-E-131-007, 114-2221-E-131-012-MY3), Chang Gung University, Taoyuan, Taiwan (URRPD2Q0041) and Chang Gung Memorial Hospital, Linkou, Taiwan (CMRPD2N0072) are highly appreciated.

Appendix A. Supplementary data

Supplementary data to this article can be found online at https://doi.org/10.1016/j.surfcoat.2025.132701.

Data availability

Data will be made available on request.

References

[1] K. Gundepudi, P.M. Neelamraju, S. Sangaraju, G.K. Dalapati, W.B. Ball, S. Ghosh, S. Chakrabortty, A review on the role of nanotechnology in the development of near-infrared photodetectors: materials, performance metrics, and potential applications, J. Mater. Sci. 58 (2023) 13889–13924.
[2] A. Qadir, S. Shafique, T. Iqbal, H. Ali, L. Xin, S. Ruibing, T. Shi, H. Xu, Y. Wang, Z. Hu, Recent advancements in polymer-based photodetector: a comprehensive review, Sens. Actuators, A 370 (2024) 115267.
[3] G. Simone, M.J. Dyson, S.C.J. Meskers, R.A.J. Janssen, G.H. Gelinck, Organic photodetectors and their application in large area and flexible image sensors: the role of dark current, Adv. Funct. Mater. 30 (2020) 1904205.
[4] H. Anabestani, S. Nabavi, S. Bhadra, Advances in flexible organic photodetectors: materials and applications, Nanomaterials (Basel) 12 (2022) 3775.
[5] Q. Wang, Y. Zhang, Z. Wei, Recent progress on organic near-infrared photodetectors: mechanism, devices, and applications, Chin. J. Chem. 41 (2023) 958–978.
[6] Z. Zhao, C. Xu, L. Niu, X. Zhang, F. Zhang, Recent Progress on broadband organic photodetectors and their applications, Laser Photonics Rev. 14 (2020) 2000262.
[7] S. Gao, X. Wang, Y. Zhao, Y. Xu, W. Qiao, Z.Y. Wang, Broadband all-polymer photodetectors with ultrahigh detectivity above 10^{14} Jones enabled by fine-tuned molecular stacking via facile random terpolymerization, Chem. Eng. J. 489 (2024) 151377.
[8] C. McDowell, M. Abdelsamie, M.F. Toney, G.C. Bazan, Solvent additives: key morphology-directing agents for solution-processed organic solar cells, Adv. Mater. 30 (2018) 1707114.
[9] J. Jing, Y. Dou, S. Chen, K. Zhang, F. Huang, Solution sequential deposited organic photovoltaics: from morphology control to large-area modules, eScience 3 (2023) 100142.
[10] Z. Du, H.M. Luong, S. Sabury, A.L. Jones, Z. Zhu, P. Panoy, S. Chae, A. Yi, H.J. Kim, S. Xiao, V.V. Brus, G.N. Manjunatha Reddy, J.R. Reynolds, T.-Q. Nguyen, High-performance wearable organic photodetectors by molecular design and green solvent processing for pulse oximetry and photoplethysmography, Adv. Mater. 36 (2024) 2310478.
[11] S. Xing, J. Kublitski, C. Hänisch, L.C. Winkler, T.-y. Li, H. Kleemann, J. Benduhn, K. Leo, Photomultiplication-type organic photodetectors for near-infrared sensing with high and bias-independent specific detectivity, Adv. Sci. 9 (2022) 2105113.
[12] L. Li, F. Zhang, J. Wang, Q. An, Q. Sun, W. Wang, J. Zhang, F. Teng, Achieving EQE of 16,700% in P3HT:$PC_{71}BM$ based photodetectors by trap-assisted photomultiplication, Sci. Rep. 5 (2015) 9181.
[13] W. Wang, F. Zhang, M. Du, L. Li, M. Zhang, K. Wang, Y. Wang, B. Hu, Y. Fang, J. Huang, Highly narrowband photomultiplication type organic photodetectors, Nano Lett. 17 (2017) 1995–2002.
[14] J. Miao, F. Zhang, M. Du, W. Wang, Y. Fang, Photomultiplication type organic photodetectors with broadband and narrowband response ability, Adv Opt Mater 6 (2018) 1800001.
[15] N. Schopp, G. Akhtanova, P. Panoy, A. Arbuz, S. Chae, A. Yi, H.J. Kim, V. Promarak, T.-Q. Nguyen, V.V. Brus, Unraveling device physics of dilute-donor narrow-bandgap organic solar cells with highly transparent active layers, Adv. Mater. 34 (2022) 2203796.
[16] Z. Liu, L. Tao, Y. Zhang, G. Zhou, H. Zhu, Y. Fang, G. Wu, D. Yang, H. Chen, Narrowband near-infrared photodetector enabled by dual functional internal-filter-induced selective charge collection, Adv Opt Mater 9 (2021) 2100288.
[17] T. Shan, X. Hou, X. Yin, X. Guo, Organic photodiodes: device engineering and applications, Front. Optoelectron. 15 (2022) 49.
[18] M.-S. Choi, S. Lee, H.J. Kim, J.-J. Kim, Inverted near-infrared organic photodetector with oriented lead (II) phthalocyanine molecules via substrate heating, Org. Electron. 61 (2018) 164–169.
[19] Y. Yao, Y. Chen, H. Wang, P. Samorì, Organic photodetectors based on supramolecular nanostructures, SmartMat 1 (2020) e1009.
[20] X. Ma, R.A.J. Janssen, G.H. Gelinck, Trap-assisted charge generation and recombination in state-of-the-art organic photodetectors, Adv. Mater. Technol. 8 (2023) 2300234.
[21] P.E. Keivanidis, P.K.H. Ho, R.H. Friend, N.C. Greenham, The dependence of device dark current on the active-layer morphology of solution-processed organic photodetectors, Adv. Funct. Mater. 20 (2010) 3895–3903.
[22] R. Meier, M.A. Ruderer, A. Diethert, G. Kaune, V. Körstgens, S.V. Roth, P. Müller-Buschbaum, Influence of film thickness on the phase separation mechanism in ultrathin conducting polymer blend films, J. Phys. Chem. B 115 (2011) 2899–2909.
[23] J.B. Park, J.-W. Ha, S.C. Yoon, C. Lee, I.H. Jung, D.-H. Hwang, Visible-light-responsive high-detectivity organic photodetectors with a 1 μm thick active layer, ACS Appl. Mater. Interfaces 10 (2018) 38294–38301.

[24] J. Huang, J. Lee, J. Vollbrecht, V.V. Brus, A.L. Dixon, D.X. Cao, Z. Zhu, Z. Du, H. Wang, K. Cho, G.C. Bazan, T.Q. Nguyen, A high-performance solution-processed organic photodetector for near-infrared sensing, Adv. Mater. 32 (2020) e1906027.
[25] C.-J. Shih, Y.-Z. Li, M.-Z. Li, S. Biring, B.-C. Huang, C.-W. Liu, T.-H. Yeh, D. Luo, J.-H. Lee, Y.-H. Huang, K.-T. Wong, S.-W. Liu, Transparent organic upconversion device targeting high- grade infrared visual image, Nano Energy 86 (2021) 106043.
[26] C. Shan, T. Liu, J. Zhou, Y. He, D. Luo, Z. Jiang, Z. Wang, Q. Liu, C.a. Li, F. Zhang, E. Zhou, K. Wang, A.K.K. Kyaw, High-performance organic solar cell and self-power photodetector with chemically robust, near-infrared acceptor enabled by strengthening interfacial contact and compositional modulation, Chem. Eng. J. 471 (2023) 144451.
[27] H.J. Eun, H. Lee, Y. Shim, G.U. Seo, A.Y. Lee, J.J. Park, J. Heo, S. Park, J.H. Kim, Strain-durable dark current in near-infrared organic photodetectors for skin-conformal photoplethysmographic sensors, iScience 25 (2022) 104194.
[28] A. Guerrero, G. Garcia-Belmonte, Recent advances to understand morphology stability of organic photovoltaics, Nano Micro Lett. 9 (2016) 10.
[29] H. Quan, Z. Zhong, T. Hao, K. An, W. Zhong, C. Wang, F. Liu, L. Ying, F. Huang, High-performance organic photodetectors enabled by a refined fibrillar multiphase morphology, Chem. Eng. J. 452 (2023) 139295.
[30] Z. Yin, S. Mei, L. Chen, P. Gu, J. Huang, X. Li, H.-Q. Wang, W. Song, Efficient PTB7-Th:Y6:$PC_{71}BM$ ternary organic solar cell with superior stability processed by chloroform, Org. Electron. 99 (2021) 106308.
[31] Y.-M. Sung, A.K. Akbar, S. Biring, C.-F. Li, Y.-C. Huang, S.-W. Liu, The effect of ZnO preparation on the performance of inverted polymer solar cells under one sun and indoor light, J. Mater. Chem. C 9 (2021) 1196–1204.
[32] J. Kublitski, A. Hofacker, B.K. Boroujeni, J. Benduhn, V.C. Nikolis, C. Kaiser, D. Spoltore, H. Kleemann, A. Fischer, F. Ellinger, K. Vandewal, K. Leo, Reverse dark current in organic photodetectors and the major role of traps as source of noise, Nat. Commun. 12 (2021) 551.
[33] F. Wang, T. Zhang, R. Xie, Z. Wang, W. Hu, How to characterize figures of merit of two-dimensional photodetectors, Nat. Commun. 14 (2023) 2224.
[34] S. Watanabe, H. Sugawara, R. Häusermann, B. Blülle, A. Yamamura, T. Okamoto, J. Takeya, Remarkably low flicker noise in solution-processed organic single crystal transistors, Commun. Phys. 1 (2018) 37.
[35] P.C.Y. Chow, T. Someya, Organic photodetectors for next-generation wearable electronics, Adv. Mater. 32 (2020) 1902045.
[36] J. Kublitski, A. Hofacker, B.K. Boroujeni, J. Benduhn, V.C. Nikolis, C. Kaiser, D. Spoltore, H. Kleemann, A. Fischer, F. Ellinger, K. Vandewal, K. Leo, Reverse dark current in organic photodetectors and the major role of traps as source of noise, Nat. Commun. 12 (2021) 551.
[37] C. Fuentes-Hernandez, W.-F. Chou, T.M. Khan, L. Diniz, J. Lukens, F.A. Larrain, V. A. Rodriguez-Toro, B. Kippelen, Large-area low-noise flexible organic photodiodes for detecting faint visible light, Science 370 (2020) 698–701.
[38] T.H. Kim, J.H. Lee, M.H. Jang, G.M. Lee, E.S. Shim, S. Oh, M.A. Saeed, M.J. Lee, B.-S. Yu, D.K. Hwang, C.W. Park, S.Y. Lee, J.W. Jo, J.W. Shim, Atto-scale noise near-infrared organic photodetectors enabled by controlling interfacial energetic offset through enhanced anchoring ability, Adv. Mater. 36 (2024) 2403647.
[39] P. Wilson, Chapter 5 - analog integrated circuits, in: P. Wilson (Ed.), The Circuit Designer's Companion, Fourth edition, Newnes, 2017, pp. 209–257.
[40] L. Shao, J. Yang, Y. Huang, Y. Cao, J. Jing, X. Qin, X. Yang, H. Tang, C. Liu, F. Huang, Y. Cao, Molecular order control of nonfullerene acceptors enables ultralow dark current and high responsivity in short-wavelength infrared organic photodetectors, Chem. Mater. 36 (2024) 5775–5787.
[41] Z. Lan, Y. Lei, W.K.E. Chan, S. Chen, D. Luo, F. Zhu, Near-infrared and visible light dual-mode organic photodetectors, Sci. Adv. 6 (2020) eaaw8065.
[42] M.Y. Hadiyanto, R. Estrada, C.-C. Lee, S. Biring, A.K. Akbar, C.-Y. Li, C.-J. Shih, Y.-Z. Li, S.-W. Liu, Transparent photodetectors with ultra-low dark current and high photoresponse for near-infrared detection, Org. Electron. 99 (2021) 106356.
[43] R. Dong, Y. Fang, J. Chae, J. Dai, Z. Xiao, Q. Dong, Y. Yuan, A. Centrone, X.C. Zeng, J. Huang, High-gain and low-driving-voltage photodetectors based on organolead triiodide perovskites, Adv. Mater. 27 (2015) 1912–1918.
[44] O. Alqahtani, S.M. Hosseini, T. Ferron, V. Murcia, T. McAfee, K. Vixie, F. Huang, A. Armin, S. Shoaee, B.A. Collins, Evidence that sharp interfaces suppress recombination in thick organic solar cells, ACS Appl. Mater. Interfaces 13 (2021) 56394–56403.
[45] Y. Xu, J. Yuan, S. Zhou, M. Seifrid, L. Ying, B. Li, F. Huang, G.C. Bazan, W. Ma, Ambient processable and stable all-polymer organic solar cells, Adv. Funct. Mater. 29 (2019) 1806747.
[46] A.C. Lazanas, M.I. Prodromidis, Electrochemical impedance spectroscopy—a tutorial, ACS Meas. Sci. Au 3 (2023) 162–193.
[47] Z. Wu, N. Li, N. Eedugurala, J.D. Azoulay, D.-S. Leem, T.N. Ng, Noise and detectivity limits in organic shortwave infrared photodiodes with low disorder, NPJ Flex. Electron. 6 (2020).
[48] Q. Jiang, L. Zhang, H. Wang, X. Yang, J. Meng, H. Liu, Z. Yin, J. Wu, X. Zhang, J. You, Enhanced electron extraction using SnO_2 for high-efficiency planar-structure $HC(NH_2)_2PbI_3$-based perovskite solar cells, Nat. Energy 2 (2016) 16177.
[49] Z. Lan, Y.S. Lau, L. Cai, J. Han, C.W. Suen, F. Zhu, Dual-band organic photodetectors for dual-channel optical communications, Laser Photonics Rev. 16 (2022) 2100602.
[50] Z. Lan, Y.S. Lau, Y. Wang, Z. Xiao, L. Ding, D. Luo, F. Zhu, Filter-free band-selective organic photodetectors, Adv Opt Mater 8 (2020) 2001388.